Article:
Iles-Smith, J., Svendsen, M.K., Rubio, A. et al. (2025) On-demand heralded MIR single-photon source using a cascaded quantum system. Science Advances, 11 (11). eadr9239. ISSN: 2375-2548

https://doi.org/10.1126/sciadv.adr9239

OPTICS

On-demand heralded MIR single-photon source using a cascaded quantum system

Jake Iles-Smith[1,2]*†, Mark Kamper Svendsen[3,4]†, Angel Rubio[3,7,8], Martijn Wubs[5,6,9], Nicolas Stenger[5,6,9]*

We propose a mechanism for generating single photons in the mid-infrared (MIR) using a solid-state or molecular quantum emitter. The scheme uses cavity quantum electrodynamics (QED) effects to selectively enhance a Frank-Condon transition, deterministically preparing a single Fock state of a polar phonon mode. By coupling the phonon mode to an antenna, the resulting excitation is then radiated to the far field as a single photon with a frequency matching the phonon mode. By combining macroscopic QED calculations with methods from open quantum system theory, we show that optimal parameters to generate these MIR photons occur for modest light-matter coupling strengths, which are achievable with state-of-the-art technologies. Combined, the cascaded system we propose provides a quasi-deterministic source of heralded single photons in a regime of the electromagnetic spectrum where this previously was not possible.

INTRODUCTION

Single photons lie at the heart of many applications in quantum science and technology. Among these applications, quantum metrology and precision spectroscopy stand out as particularly promising, because they can, in principle, reach the so-called quantum limit of precision in transmission and absorption spectroscopy (*1*–*4*). This approach holds particular promise in the context of spectroscopy of biological systems (*5*–*8*), where stringent power limitations are imposed on conventional spectroscopic techniques to prevent damage of biological samples.

The range of degrees of freedom that can be explored through single-photon spectroscopy is intricately tied to the frequency of the generated photons. Specifically, single photons in the visible spectrum are instrumental in investigating electronic processes, whereas photons in the mid-infrared (MIR) and far-infrared (IR) ranges are indispensable for probing vibrational transitions. Quantum light sources in the MIR could enable precise measurements in vivo on the single molecular vibration level, understand the fundamental role played by vibrations in quantum matter (*9*), and give us the spectroscopic means to follow chemical reactions in solvents (*10*, *11*). While there have been important developments in pushing single-photon sources to the near IR and telecommunication C-bands (*12*, *13*), these quantum emitters (QEs) rely on well-defined electronic transitions and, thus, are not able to access the spectral regimes relevant to vibrational transitions. So far, there are no known materials with bandgaps in the MIR able to efficiently produce single photons with high brightness.

In this work, we propose a scheme for generating single photons in the MIR using a QE interacting with polar phonon modes, an optical cavity, and a MIR antenna. The protocol consists of a two-part cascaded process that is shown schematically in Fig. 1: In the first stage, a single Fock state ($|1\rangle$) is prepared in the polar phonon mode through the selective Purcell enhancement of the first phonon sideband (PSB). As shown schematically in Fig. 1A, the successful preparation of the single phonon state is heralded by the emission of an optical photon. The preparation and manipulation of such quantum vibrational states is of notable interest to applications in quantum optomechanics and transduction. However, existing proposals are inherently probabilistic (*14*–*16*) and demand advanced time-resolved spectroscopic schemes (*17*). In contrast, our protocol can be implemented deterministically with standard photonic/plasmonic cavities if the sideband corresponding to the relevant phonon mode can be spectrally isolated, and crucially is heralded by the emission of a photon via the cavity mode.

In the second stage of our protocol, the excitation in the phonon mode is radiated as a photon by coupling the phonon mode to a resonant antenna structure (*18*–*20*), as shown in Fig. 1B. By starting with a macroscopic quantum electrodynamics (QED) description of the QE and phonon environment, we show that the macroscopic dipole moment of the polar phonon mode enables efficient transfer of excitation to the antenna structure, which is subsequently radiated as a single photon with the same frequency as the phonon mode. Such antennas can be constructed from plasmonic nanostructures (*21*) in both the visible and IR (*22*), and allow for the bright emission of single photons into the far field (*23*, *24*). A similar coupling has been proposed by Terry Weatherly *et al.* (*25*) as a means to down-convert classical driving fields from visible to IR frequencies. In contrast to a recent proposal for generating single photons in the MIR (*26*), our scheme does not rely on continuous external field driving of the emitter in the strong coupling regime. Instead, in our structure, the emission of the MIR photon is heralded by the detection of a single photon in the visible range, which is generated by a PSB transition that is selectively Purcell enhanced via a resonant optical

[1]School of Mathematical and Physical Sciences, The University of Sheffield, Sheffield S10 2TN, UK. [2]Department of Physics and Astronomy, The University of Manchester, Manchester M13 9PL, UK. [3]Department of Physics, Max Planck Institute for the Structure and Dynamics of Matter and Center for Free-Electron Laser Science, Luruper Chaussee 149, 22761 Hamburg, Germany. [4]NNF Quantum Computing Programme, Niels Bohr Institute University of Copenhagen, Copenhagen, Denmark. [5]Department of Electrical and Photonics Engineering, Technical University of Denmark, 2800 Kgs. Lyngby, Denmark. [6]Center for Nanostructured Graphene, Technical University of Denmark, 2800 Kgs. Lyngby, Denmark. [7]Center for Computational Quantum Physics, Flatiron Institute, New York, NY 10010, USA. [8]Nano-Bio Spectroscopy Group and European Theoretical Spectroscopy Facility (ETSF), Universidad del País Vasco (UPV/EHU), Av. Tolosa 72, 20018 San Sebastian, Spain. [9]NanoPhoton–Center for Nanophotonics, Technical University of Denmark, 2800 Kgs. Lyngby, Denmark.
*Corresponding author. Email: jake.iles-smith@sheffield.ac.uk (J.I.-S.); niste@dtu.dk (N.S.)
†These authors contributed equally to this work.

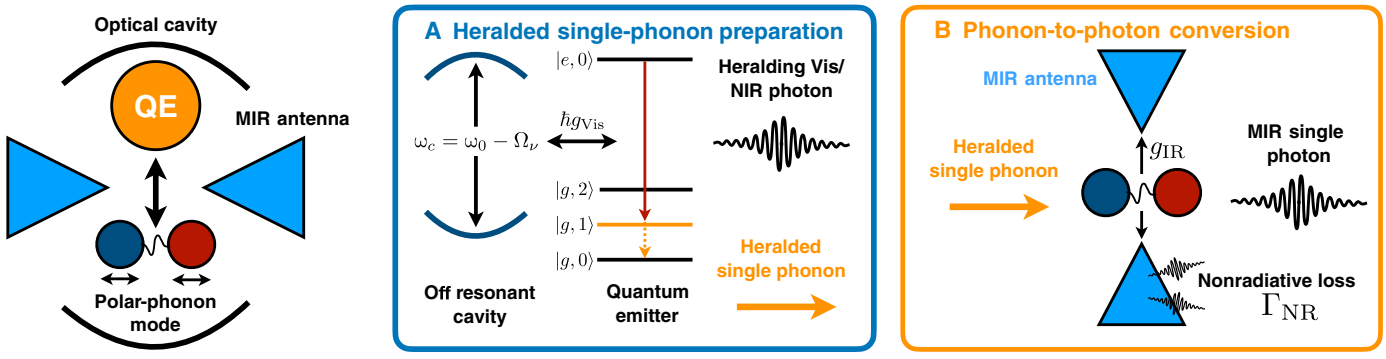

Fig. 1. A schematic of the MIR-photon generation protocol. (Left) Schematic of a quantum emitter (QE) with energy $\hbar\omega_0$ coupled to an optical cavity with energy $\hbar\omega_c$ and light-matter coupling strength $\hbar g_{\mathrm{Vis}}$, interacting with a polar phonon mode of energy $\hbar\Omega_\nu$. The phonon mode is then coupled to a plasmonic or dielectric antenna tuned to its resonance, with coupling strength g_{IR}. The middle and right panels show the two-step photon generation protocol: (**A**) An initially excited quantum emitter emits a photon in the visible via the first PSB, which is Purcell enhanced through the cavity interaction. The emitted photon is used to herald the generation of a single phonon. (**B**) The phonon then radiates as a single MIR photon through the interaction with the MIR antenna structure.

cavity. Furthermore, our scheme is not restricted to a particular material system, and is applicable to any QE, solid state or molecular, coupled to polar phonons.

The manuscript is organized as follows: We first derive a Hamiltonian for the emitter-phonon-antenna system that underpins our protocol using macroscopic QED., before characterizing the performance of the two-step cascaded system, including generation efficiency and purity of the resulting emitted photon in the MIR. We conclude the paper by discussing how the protocol can be realized in material-based systems, including defects in two-dimensional (2D) materials, inorganic nanocrystals, and molecular systems.

RESULTS

Model for a cascaded QE in the mid IR

We start by considering a molecular system, with electronic and nuclear degrees of freedom governed by the Hamiltonian $\hat{H}_{\mathrm{mol}}$. Within the length gauge, the interaction between the molecule and the electromagnetic (EM) degrees of freedom are given by (*27*, *28*)

$$\hat{H} = \hat{H}_{\mathrm{mol}} + \frac{1}{2}\sum_{\alpha=1}^{N}\left(\hat{p}_\alpha^2 + \omega_\alpha^2\left[\hat{q}_\alpha + \frac{\boldsymbol{\lambda}_\alpha}{\omega_\alpha}\cdot\hat{\boldsymbol{\mu}}_{\mathrm{total}}\right]^2\right) \tag{1}$$

where ω_α, $\hat{p}_\alpha$, and $\hat{q}_\alpha$ are the frequency, momentum, and displacement operators associated with photon mode α, respectively. The total dipole moment can be decomposed into a sum of the nuclear and electronic dipole moments, $\hat{\boldsymbol{\mu}}_{\mathrm{total}} = \hat{\boldsymbol{\mu}}_{\mathrm{nu}} + \hat{\boldsymbol{\mu}}_{\mathrm{el}}$. The coupling between the molecular degrees of freedom and the EM field occurs through the matrix elements $\boldsymbol{\lambda}_\alpha$. These matrix elements can be related to the dyadic Green's function of the EM environment in a quantitative way and generally reflect the dipole spectral density of the EM environment (*29*). We discuss this relation and its implication for realistic structures in the Supplementary Materials.

As our model of the intramolecular Hamiltonian, we consider a single polar phonon mode coupled to a two-level molecule, with ground and excited states, $|g\rangle$ and $|e\rangle$, respectively. In the diabatic basis, and assuming linear electron-phonon coupling, the molecular Hamiltonian takes the form (*25*)

$$\hat{H}_{\mathrm{mol}} = \left[E_{\mathrm{vert}} - \Omega_\nu Q_e^{(0)}\hat{Q}_\nu\right]|e\rangle\langle e| + \frac{1}{2}\left(\hat{P}_\nu^2 + \Omega_\nu^2\hat{Q}_\nu^2\right) \tag{2}$$

Here, Ω_ν is the frequency of the polar phonon mode, and $\hat{Q}_\nu$ ($\hat{P}_\nu$) is the phonon configurational coordinate displacement (momentum) operator. $Q_e^{(0)}$ is the configurational coordinate displacement along that phonon mode associated with the minimum of the excited state potential energy surface (PES) relative to that of the ground state. The transition energy associated with the ground and excited state is given by $E_{\mathrm{vert}} = \hbar\omega_{\mathrm{eg}} + S\hbar\Omega_\nu$, where $S = \left[Q_e^{(0)}\right]^2/\left(2\hbar\Omega_\nu\right)$ is the Huang-Rhys parameter, and $\hbar\omega_{\mathrm{eg}}$ is the energy difference between the minima of the ground- and excited state PES.

We can express the molecular Hamiltonian within second quantization notation, using $\hat{Q}_\nu = \sqrt{\hbar/2\Omega_\nu}\left(\hat{b}^\dagger + \hat{b}\right)$, such that

$$\hat{H}_{\mathrm{mol}} = \left[E_{\mathrm{vert}} - \hbar\eta_\nu\left(\hat{b}^\dagger + \hat{b}\right)\right]|e\rangle\langle e| + \hbar\Omega_\nu\hat{b}^\dagger\hat{b} \tag{3}$$

where we have defined $\hbar\eta_\nu = Q_e^{(0)}\sqrt{\hbar\Omega_\nu/2}$.

Coupling the electron-phonon system to the EM environment

To study the impact of the EM environment on the coupled electron-nuclear system, we can expand the dipole operator in the diabatic basis. The electronic dipole operator takes the standard form $\hat{\boldsymbol{\mu}}_{\mathrm{el}} = \boldsymbol{\mu}_{eg}\hat{\sigma}_x$, where we have defined the Pauli operator $\hat{\sigma}_x = \left(|e\rangle\langle g| + \mathrm{h.c.}\right)$ and neglected the permanent dipole contribution. The nuclear dipole moment, up to first order in the phonon displacement and neglecting the permanent dipole moment of the atomic lattice, is $\hat{\boldsymbol{\mu}}_{\mathrm{nu}}\left(\hat{Q}_\nu\right) \approx \boldsymbol{\mu}_{\mathrm{N}}\sqrt{\frac{2\Omega_\nu}{\hbar}}\left[\hat{Q}_\nu - Q_g^{(0)}\right]$, where $\boldsymbol{\mu}_{\mathrm{N}}$ describes the magnitude of the nuclear dipole moment, and may be related to the Born charges of the system as will be shown later. The above operator describes the change of the dipole moment due to the displacement along the phonon mode, which leads to IR activity.

With an expression for the dipole moment operator in hand, we can consider the coupling to the EM environment, which we assume consists of two parts, as shown schematically in Fig. 1: a single-mode optical cavity in the visible range with mode frequency ω_{Vis} and a MIR antenna with frequency ω_{MIR}. As shown by Kats *et al.* (*18*), it is often well justified to approximate the antenna structure by a single damped mode. Both single-mode EM environments are

defined by the displacement (momentum) operators $\hat{q}_\alpha$ ($\hat{p}_\alpha$) with $\alpha = \mathrm{Vis}, \mathrm{MIR}$. Using the Hamiltonian Eq. 1, and expanding the dipole moment operator, we have

$$\hat{H} = \hat{H}_{\mathrm{mol}} + \sum_{\alpha=\mathrm{Vis,IR}} \frac{1}{2}\left(\hat{p}_\alpha^2 + \omega_\alpha^2 \hat{q}_\alpha^2\right) + \omega_{\mathrm{Vis}} \boldsymbol{\lambda}_{\mathrm{Vis}} \hat{q}_{\mathrm{Vis}} \hat{\boldsymbol{\mu}}_{\mathrm{el}} + \omega_{\mathrm{IR}} \boldsymbol{\lambda}_{\mathrm{IR}} \hat{q}_{\mathrm{IR}} \hat{\mu}_{\mathrm{nu}} + \frac{\left(\boldsymbol{\lambda}_{\mathrm{Vis}} \cdot \hat{\boldsymbol{\mu}}_{\mathrm{Tot}}\right)^2 + \left(\boldsymbol{\lambda}_{\mathrm{IR}} \cdot \hat{\boldsymbol{\mu}}_{\mathrm{Tot}}\right)^2}{2} \tag{4}$$

Because the optical and MIR transitions are far off-resonance, we have neglected the coupling between the electronic-dipole transition and the MIR antenna, and similarly for the phonon mode and the optical cavity. The final term in Eq. 4 is the dipole self-energy term. In our construction, it will contain three different contributions: the electronic-, the nuclear-, and the cross nuclear–electronic dipole self-energies. In general, keeping all these contributions is crucial to ensure the stability of the coupled system and the existence of a ground state (*30*). However, under the two-level approximation that we apply in this work, the electronic contribution is proportional to $\hat{\sigma}_x^2 = \mathbb{I}_2$, and it thus manifests as a simple energy shift of both the ground and excited states. The electronic contribution can therefore be safely neglected in our setting.

We now move to a second quantized notation, such that $\hat{q}_\alpha = \sqrt{\hbar / 2\omega_\alpha}\left(\hat{a}_\alpha^\dagger + \hat{a}_\alpha\right)$, yielding the Hamiltonian

$$\hat{H} = \hat{H}_{\mathrm{mol}} + \sum_{\alpha=\mathrm{V,IR}} \hbar\omega_\alpha \hat{a}_\alpha^\dagger \hat{a}_\alpha + \hbar g_{\mathrm{Vis}} \hat{\sigma}_x \left(\hat{a}_{\mathrm{Vis}} + \hat{a}_{\mathrm{Vis}}^\dagger\right) + \hbar g_{\mathrm{IR}} \left(\hat{b}^\dagger + \hat{b}\right)\left(\hat{a}_{\mathrm{IR}} + \hat{a}_{\mathrm{IR}}^\dagger\right) + \hbar\eta_c \hat{\sigma}_x \left(\hat{b}^\dagger + \hat{b}\right) + \hbar\delta_c \left(\hat{b}^\dagger + \hat{b}\right)^2$$

Here, we have introduced the standard light-matter coupling strengths (*29*)

$$\hbar g_{\mathrm{Vis}} = \sqrt{\frac{\hbar\omega_{\mathrm{Vis}}}{2}} \boldsymbol{\mu}_{eg} \cdot \boldsymbol{\lambda}_{\mathrm{Vis}} \tag{5}$$

$$\hbar g_{\mathrm{IR}} = \sqrt{\frac{\hbar\omega_{\mathrm{IR}}}{2}} \boldsymbol{\mu}_{N} \cdot \boldsymbol{\lambda}_{\mathrm{IR}} \tag{6}$$

and the counter-term energies

$$\eta_c = 2\left(\frac{g_{\mathrm{Vis}}^2}{\omega_{\mathrm{Vis}}} \frac{\mu_{\mathrm{N}}}{\mu_{eg}} + \frac{g_{\mathrm{IR}}^2}{\omega_{\mathrm{IR}}} \frac{\mu_{eg}}{\mu_{\mathrm{N}}}\right) \tag{7}$$

$$\delta_c = \frac{g_{\mathrm{IR}}^2}{\omega_{\mathrm{IR}}} + \frac{g_{\mathrm{Vis}}^2}{\Omega_{\mathrm{Vis}}} \left(\frac{\mu_{\mathrm{N}}}{\mu_{eg}}\right)^2 \tag{8}$$

where we have introduced $\mu_\alpha = |\boldsymbol{\mu}_\alpha|$. Note that the counter term stemming from the electron-nuclear dipole self-energy contribution, the term proportional to $\hat{\sigma}_x\left(\hat{b}^\dagger + \hat{b}\right)$, will be heavily suppressed because the phonon mode and optical transition are far detuned from one another. We therefore neglect this term. Furthermore, because the IR frequency is substantially lower than the visible frequency and the nuclear dipole moments are one to two orders of magnitude smaller than electronic dipole moments, the counter term is dominated by its first term $\delta_c \approx g_{\mathrm{IR}}^2 / \omega_{\mathrm{IR}}$.

Last, because the frequency associated to the optical transition is much larger than any other energy scale, we can make the rotating wave approximation, placing the visible cavity coupling in Jaynes-Cummings form

$$\hat{H} \approx \hat{H}_{\mathrm{mol}} + \sum_{\alpha=\mathrm{V,IR}} \hbar\omega_\alpha \hat{a}_\alpha^\dagger \hat{a}_\alpha + \hbar g_{\mathrm{Vis}} \left(\hat{\sigma}^\dagger \hat{a}_{\mathrm{Vis}} + \hat{\sigma} \hat{a}_{\mathrm{Vis}}^\dagger\right) + \hbar g_{\mathrm{IR}} \left(\hat{b}^\dagger + \hat{b}\right)\left(\hat{a}_{\mathrm{IR}} + \hat{a}_{\mathrm{IR}}^\dagger\right) + \hbar\delta_c \left(\hat{b}^\dagger + \hat{b}\right)^2 \tag{9}$$

Master equation for the cascaded MIR source

With the Hamiltonian for the cascaded system now established, we can proceed to analyze its dynamics using the master equation formalism. This approach allows us to incorporate the finite lifetimes of the cavity, antenna, and phonon modes, which are characterized by their spectral widths, denoted as κ_{Vis}, κ_{IR}, and γ, respectively. Here, $\kappa_{\mathrm{IR}} = \Gamma_{\mathrm{R}} + \Gamma_{\mathrm{NR}}$ includes both a radiative contribution Γ_{R}, which represents energy loss to the far field, and a nonradiative contribution Γ_{NR}, which accounts for internal losses in the antenna.

In our study, we focus specifically on quasi-localized phonon and EM modes and we consider operating at cryogenic temperatures. These modes are well described by Lorentzian profiles, where the width corresponds directly to the finite lifetime of each mode. Such modes can be formally represented as single-bosonic modes with Lindblad-type dissipation (*31*–*33*). Therefore, we define the master equation in the following form

$$\frac{\partial \rho(t)}{\partial t} = -\frac{i}{\hbar}\left[\hat{H}, \rho(t)\right] + \frac{\kappa_{\mathrm{Vis}}}{2}\mathcal{L}_{\hat{a}_{\mathrm{Vis}}}\left[\rho(t)\right] + \frac{\kappa_{\mathrm{IR}}}{2}\mathcal{L}_{\hat{a}_{\mathrm{IR}}}\left[\rho(t)\right] + \frac{\gamma}{2}\mathcal{L}_{\hat{b}}\left[\rho(t)\right] \tag{10}$$

Here, $\rho(t)$ represents the reduced density operator of the electronic-cavity-antenna-phonon system, and the Lindblad dissipator $\mathcal{L}_{\hat{O}}[\rho]$ is defined as $\mathcal{L}_{\hat{O}}[\rho] = 2\hat{O}\rho\hat{O}^\dagger - \hat{O}^\dagger\hat{O}\rho - \rho\hat{O}^\dagger\hat{O}$. The EM loss rates, κ_{Vis} and κ_{IR}, arise from the coupling between localized EM modes and the external field, with their values determined by the quality factors of the respective modes, which are determined by the design of the surrounding EM structures. The intrinsic decay rate of the phonon mode, γ, is due to phonon interactions with background modes in the material. Although this description of phonon modes via Lindblad dissipation appears simplistic, it has proven remarkably effective. For instance, comparisons between experimental results and theoretical models of local phonon modes, as seen in studies on organic molecules (*34*) and defect centers in hexagonal boron nitride (hBN) (*35*), demonstrate excellent agreement with spectra obtained from experiments. The precise value of the phonon intrinsic loss rate (or, equivalently, its lifetime) is material dependent, and further discussion of this parameter is given at the end of the results section. Note that we also assume that thermal excitation of the phonon mode is negligible, i.e., that the splitting of the phonon mode $\hbar\Omega_\nu$ exceeds the background thermal energy. This is a good approximation for optical phonon modes, because their energies tend to be in the 10- to 200-meV range, which far exceeds thermal energies at cryogenic temperatures.

Solving this master equation numerically enables us to extract the optical properties of the composite system across both the IR and visible spectral regimes. As shown schematically in Fig. 1, to generate a single photon in the MIR, we first need to generate an optical photon, which deterministically prepares a single phonon state, before converting this phonon state into a MIR photon. In the next sections, we shall consider each step in the process independently to illustrate the mechanisms involved, before combining them as a single cascaded process.

Single phonon generation

We start by considering the process by which a single phonon state is deterministically prepared. To illustrate this, we initially consider a phonon mode in the absence of the MIR antenna and intrinsic losses (i.e., $g_{IR} = \gamma = 0$). We consider the QE to be initially prepared in its excited state, with the phonon mode prepared in the ground state of the PES associated with the excited electronic configuration, i.e., the coherent state $|S\rangle = |\eta_\nu / \Omega_\nu\rangle$, and with the cavity in the vacuum state.

While the pure initial state may be considered an approximation, it is well justified for the setup under consideration. The protocol is intended to operate at cryogenic temperatures, where localized phonon modes with energies well above the background thermal energy can remain in the ground state to a good approximation. Moreover, state-of-the-art driving protocols (*36*) have demonstrated near-unity excitation efficiencies, as shown in both semiconductor quantum dots (*37*) and tin-vacancy centers in diamond (*38*). As we will discuss later, the protocol is also robust against failed electronic excitation attempts. The successful generation of a single-phonon state is heralded by the detection of a visible photon emitted via the cavity, providing a reliable postselection mechanism.

Upon emitting a photon through the cavity, the resulting state of the phonon mode will be dependent on the cavity parameters. In the absence of the cavity, the emission behavior is governed by the Frank Condon principle, in which each transition is weighted by the overlap between phonon states associated to the ground- and excited-state PES, that is, $\chi_n = <S|n>^2$, where $|n\rangle$ are the Fock states associated to the electronic ground state configuration.

However, an optical cavity can suppress or enhance optical transitions depending on the cavity parameters. For example, a cavity resonant with the zero-phonon line (ZPL) ($\Delta_V = 0$) will enhance emission through the ZPL while suppressing PSB processes. This is an effect commonly used by the on-demand single photon source community to enhance an emitter's indistinguishability and efficiency (*39*–*41*). The blue curves in Fig. 2 (A to C) show the dynamics for the optical cavity, emitter, and phonon mode, respectively, with a cavity that is on resonance with the ZPL in the bad-cavity limit. Here, we see a Purcell-enhanced exponential decay from the emitter, where excitation is transferred to the cavity mode. If we consider the phonon occupation in Fig. 2C, we see that from an initial phonon occupation given by the displacement of the initial coherent state, $\langle \hat{b}^\dagger \hat{b} \rangle_{t=0} = \left(\eta_\nu / \Omega_\nu\right)^2 = 0.25$, the phonon occupation drops to the ground state of the PES associated to the ground electronic configuration. Thus, by enhancing the ZPL transition, we quasi-deterministically prepare a phonon in its ground state $|g, 0\rangle$ in the long-time limit.

Within this protocol, we wish to deterministically generate a single phonon state. We do this by red detuning the visible cavity to the first PSB transition ($\Delta_V = \Omega_\nu$), selectively enhancing the $|e, S\rangle \rightarrow |g, 1\rangle$ transition as shown schematically in Fig. 1A, while suppressing other emission channels. As shown in Fig. 2 (A and B) by the orange curves, this results in a smaller emission rate than for a resonant cavity, as the dipole transition rate is reduced by the Frank-Condon factor χ_1. In contrast to the $\Delta_V = 0$, the phonon population increases as a function of time, trending to unity in the long-time limit, indicating that the $|g, 1\rangle$ state is populated.

When intrinsic loss processes are included for the phonon mode, i.e., $\gamma \neq 0$, the phonon population now has a finite lifetime and, thus, decays to the ground state in the long-time limit, as shown by the dashed curve in Fig. 2C. However, there remains a substantial increase in phonon occupation at early times, suggesting that $|g, 1\rangle$ is still prepared. Figure 2D shows the maximum population in the first Fock state in the ground-state manifold (i.e., $|g, 1\rangle$) as a function of cavity widths for a range of coupling strengths. We see that the maximum population monotonically increases with both increasing light-matter coupling strength (g_{Vis}) and decreasing cavity width (κ_{Vis}). Note, however, that while this maximum population is not unity, this is not a true reflection of the efficiency of the preparation scheme. The cavity drives population through the $|g, 1\rangle$ state, while intrinsic losses deplete the phonon occupation; even in regimes where the losses are high, and thus the maximum phonon occupation is low, the population may still move through the $|g, 1\rangle$ state. Therefore, so long as the phonon–to–MIR photon conversion is faster than the intrinsic losses, then the conversion efficiency may still approach unity. We will discuss this in the following section.

Note that while we have focused on single-phonon state preparation, a similar strategy can be used to prepare multiphonon Fock states. By tuning the optical cavity to the *N*th-PSB, one can prepare the phonon mode to be in the state $|N\rangle$ after photon emission. With

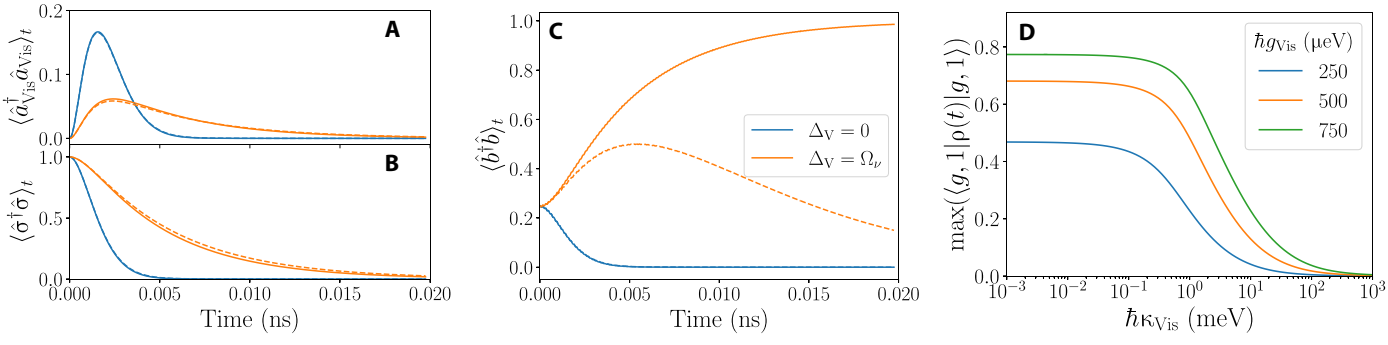

Fig. 2. Dynamical preparation of a single phonon state. (**A**) and (**B**) show the cavity occupation and emitter dynamics, respectively, for a cavity tuned to the ZPL (blue) and first sideband transition (orange) resonant. The dashed curves show the effect of including intrinsic loss of the phonon mode. Parameters used here are $\hbar g_{Vis} = 500$ μeV, $\hbar \kappa_{Vis} = 1.5$ meV, $\hbar \Omega_\nu = 180$ meV, and $\hbar \eta_\nu = 90$ meV. The intrinsic losses of the phonon mode is either = 0 (solid curves) or = 0.1 meV. (**C**) The phonon occupation for the ZPL and first sideband enhanced emission with (dashed) and without (solid) intrinsic losses in the phonon mode. Δ_V is the frequency detuning between the cavity and the ZPL. (**D**) The maximum transient population of the first Fock state in the ground-state manifold. The intrinsic loss parameter of the phonon mode is set to $\hbar \gamma = 0.1$ meV.

the extraction process described in the subsequent section, it is then possible to generate $|N\rangle$-photon states in the MIR.

Converting single phonon states to MIR photons

In the second part of the protocol illustrated in Fig. 1B, we examine the efficiency of radiating a single phonon state as a MIR photon through its interaction with an MIR antenna, following the mechanism outlined above. We start by tuning the MIR antenna to be resonant with phonon mode ($\omega_{IR} = \Omega_\nu$) and take the emitter and cavity modes to be in their ground states. The phonon mode is then initialized in the single-excitation Fock state $|1\rangle$. Figure 3A shows the phonon mode occupation as a function of time both with (solid) and without (dashed) intrinsic losses γ for several different MIR cavity parameters. Here, we see a relaxation of the phonon population to the ground state, the rate of which is Purcell enhanced by the MIR cavity. This behavior is reflected in the dynamics of the MIR antenna, as shown by Fig. 3B, where we see population accumulating in the antenna before decaying exponentially. As expected, the total occupation in the MIR antenna is reduced when intrinsic losses of the phonon mode are incorporated.

It is clear that the occupation of the MIR antenna is sensitive to both the cavity parameters, intrinsic loss of the phonon mode, and the nonradiative loss of the antenna. Therefore, it is necessary to consider the efficiency with which MIR phonons are converted to MIR photons. The key metric for the antenna is the antenna efficiency, $\eta_{ant} = \Gamma_R / \kappa_{IR}$. It describes the fraction of the phonon excitations that are radiated to the far field as MIR photons (*42*). In addition to dissipation in the antenna, it is important to account for the intrinsic phonon dissipation. In analogy with the efficiency defined in cavity QED (*41*), we therefore define the MIR phonon-to-photon efficiency as

$$\varepsilon = \frac{\eta_{ant}\kappa_{IR}\mathcal{P}_{MIR}}{\gamma\mathcal{P}_{ph-bath} + \kappa_{IR}\mathcal{P}_{MIR}} \tag{11}$$

where we have defined the powers as

$$\mathcal{P}_{MIR} = \int_0^\infty \langle a_{IR}^\dagger a_{IR}\rangle_t \, dt \text{ and } \mathcal{P}_{ph-bath} = \int_0^\infty \langle b^\dagger b\rangle_t \, dt \tag{12}$$

Notice that when the dissipation into the phonon bath can be ignored ($\gamma \approx 0$), the conversion efficiency reduces to the antenna efficiency, η_{ant}. The efficiency, as defined by Eq. 11, is plotted in Fig. 3C as a function of MIR coupling strength and intrinsic losses of the phonon mode for an idealized MIR antenna with $\Gamma_{NR} = 0$. Here, we see that there is clear competition between the intrinsic losses of the phonon mode and the Purcell-enhanced emission rate through the MIR antenna determined by the MIR coupling strength $\hbar g_{IR}$. To ensure efficient conversion of the phonon to a MIR photon, the Purcell-enhanced emission rate must exceed the intrinsic losses of the phonon mode. For small values of γ, almost unity efficiency can be achieved with moderate values of the coupling strength g_{IR}. However, as the intrinsic loss of the phonon increases, one needs increasingly strong phonon-antenna couplings to remove the excitation via the MIR antenna. For example, for an intrinsic loss rate of $\gamma = 1$ meV, corresponding to a phonon lifetime of 0.7 ps, efficiencies of phonon-photon conversion exceeds 89% for coupling strength $\hbar g_{IR} = 10$ meV. Efficient conversion in this system relies on the rapid, unidirectional transfer of phonons to the MIR antenna. This requires large light-matter coupling strengths, which are experimentally feasible, and a low Q factor for the IR mode. The large coupling ensures that the phonon energy can be effectively transferred to the EM mode, while the low Q factor of the MIR mode facilitates faster energy dissipation into the far field, preventing backflow into the phonon system and ensuring efficient energy conversion.

To account for imperfect antenna efficiency of the MIR antenna, one can scale the absolute efficiency by the fraction of photons emitted through the radiative path, as can be seen in Eq. 11. We refer the reader to the Supplementary Materials for a consideration of the impact of nonradiative antenna losses on the MIR conversion efficiency.

A final consideration for the efficacy of the MIR photon generation is the purity of the resulting photons, i.e., the degree of antibunching of the emitted MIR photons. We can determine this by considering the second-order correlation function of the cavity, such that

$$g^{(2)}(\tau) = N\int_0^\infty \left\langle a_{IR}^\dagger(t)a_{IR}^\dagger(t+\tau)a_{IR}(t+\tau)a_{IR}(t)\right\rangle dt \tag{13}$$

where $N^{-1} = \mathcal{P}_{MIR}^2$ is a normalization constant. The degree of bunching can be calculated from the coincidence counts at zero time delay, that is, $g^{(2)}(\tau = 0)$. This is shown in Fig. 4A, which shows the MIR photons with antibunching several orders of magnitude below the classical limit (shown by the dashed red curve) for all parameters chosen. This implies that the photons emitted from the MIR cavity are highly antibunched.

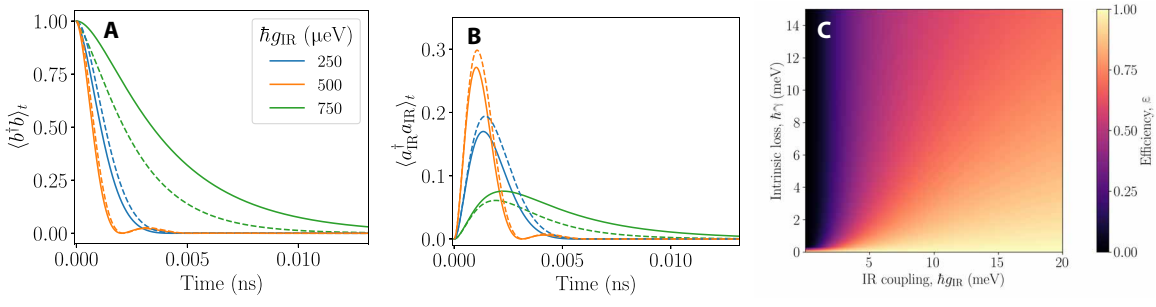

Fig. 3. The dynamics and efficiency of converting a single phonon into a MIR photon. (**A**) The occupation dynamics of the phonon mode when initialized on the $|1\rangle$ state with (dashed) and without (solid) intrinsic losses and an antenna loss rate of $\hbar\kappa_{IR} = 1.5$ meV and phonon loss = 0.1 meV. (**B**) The corresponding population dynamics of the MIR cavity mode. (**C**) The conversion efficiency of a phonon to an MIR photon as defined by Eq. 11 as a function of the intrinsic loss of the phonon mode γ and coupling strength to the MIR cavity mode g_{IR}. The efficiency was calculated with a loss rate of the MIR cavity of $\kappa_{IR} = 65$ meV with $\Gamma_{NR} = 0$. Other parameters are $\hbar g_{Vis} = 0.5$ meV, $\hbar\kappa_{Vis} = 1.5$ meV, and $\omega_{IR} = \Omega_\nu$. All other phonon parameters are the same as in Fig. 2.

Heralded MIR photon generation

Before considering realistic material parameters and systems, we wish to confirm that the MIR photon can be heralded by the emission of a photon from the optical cavity. To do this, we consider the cross-correlation function

$$g^{(2)}_{\mathrm{Her}}(\tau) = N \int_0^\infty \left\langle a^\dagger_{\mathrm{Vis}}(t) a^\dagger_{\mathrm{IR}}(t+\tau) a_{\mathrm{IR}}(t+\tau) a_{\mathrm{Vis}}(t) \right\rangle dt \qquad (14)$$

where $N^{-1} = \mathcal{P}_{\mathrm{Vis}}\mathcal{P}_{\mathrm{MIR}}$ is a normalization constant. For the MIR photon to be heralded by the visible photon, $g^{(2)}_{\mathrm{Her}}(\tau)$ should be strongly bunched, that is, at zero time delay, we expect super-Poissonian statistics in the cross-correlation measurements $g^{(2)}_{\mathrm{Her}}(0) > 1$. Figure 4B shows this behavior for different values of the IR coupling strength g_{IR} and a fixed intrinsic loss rate of $\hbar\gamma = 1$ meV. Here, we see distinct behavior depending on the value of g_{IR}: For the weakest coupling ($\hbar g_{\mathrm{IR}} = 1$ meV), there is an initial value of bunching, which becomes stronger with increasing τ, suggesting a delay between detecting the heralding photon and the MIR emission. For increasing g_{IR}, and thus Purcell enhancement, this delay is suppressed and the initial bunching increases; this is a consequence of a faster conversion from phonon to MIR photon.

We note in passing that a commercially available single-photon detector can achieve resolutions on the tens of picoseconds timescales. This suggests that even for weaker coupling strengths, the heralding efficiency can still be high. However, owing to the rapid improvement in single-photon detector technologies and ultrafast spectroscopies, strong variations as seen in Fig. 4B in the heralding efficiency could be resolved in the future.

The bunching of the visible and mid-IR photons is also affected by the intrinsic loss of the phonon mode, as shown by Fig. 4C, where we observe a decrease in the bunching $g^{(2)}_{\mathrm{Her}}(0)$ with increasing γ. This reflects a drop in the MIR photon generation efficiency, which consequently reduces the photon heralding efficiency. However, similar to our efficiency metric, the heralding success rate can be greatly improved by increasing the coupling strength (and thus Purcell enhancement) between the phonon mode and the MIR antenna.

Realistic parameters for solid-state QEs

In this section, we will assess the material parameters of well-known QEs to gauge the experimentally viable coupling strengths between polar phonon modes and an MIR antenna. The interaction between an antenna and a phonon mode is primarily influenced by two factors: the electric field strength generated by the plasmonic or photonic structure and the macroscopic polarization of the material system stemming from the polar phonon mode. Engineering efforts can enhance the electric-field strength through reduction in the mode volume. This can be achieved in nanometer-sized gapped metallic structures, as seen in plasmonic cavities (*19*, *43*, *44*), or by computer-aided design in dielectric structures to confine EM field modes (*45*–*49*). Furthermore, the polarizability of a phonon mode is intrinsically tied to the chosen material platform.

In the following, we will focus on three distinct platforms for in-depth analysis: color centers in monolayer hBN, colloidal quantum dots, and organic molecules. Each platform offers unique properties and challenges in terms of phonon-antenna coupling strength, primarily due to their material-specific polarizability and phonon modes.

Estimating the effective dipole moment of a single phonon

For a bulk material, the polarization density induced by the excitation of phonon mode *i* can be expressed as (*50*)

$$\Delta \boldsymbol{P}_i = \frac{1}{\Omega} \sum_{\alpha}^{N} Z_\alpha \varepsilon_{i\alpha} \qquad (15)$$

Here, Z_α is the Born effective charges of atom α and $\varepsilon_{i\alpha}$ is the displacement of atom α due to the phonon mode *i*. Ω is the unit cell volume and N is the number of atoms in the unit cell. [In this work, we calculate the Born effective charges using the GPAW and ASE codes (*51*–*53*). Details of these simulations can be found in the Supplementary Materials.] Equation 15 tells us that to have an induced polarization by a phonon mode, we need (i) a polar crystal (otherwise, $Z_\alpha = 0 \ \forall \ \alpha$) and (ii) a phonon mode, which displaces the atoms such that their overall displacement results in a net movement of charge. In addition to the Born effective charges and the

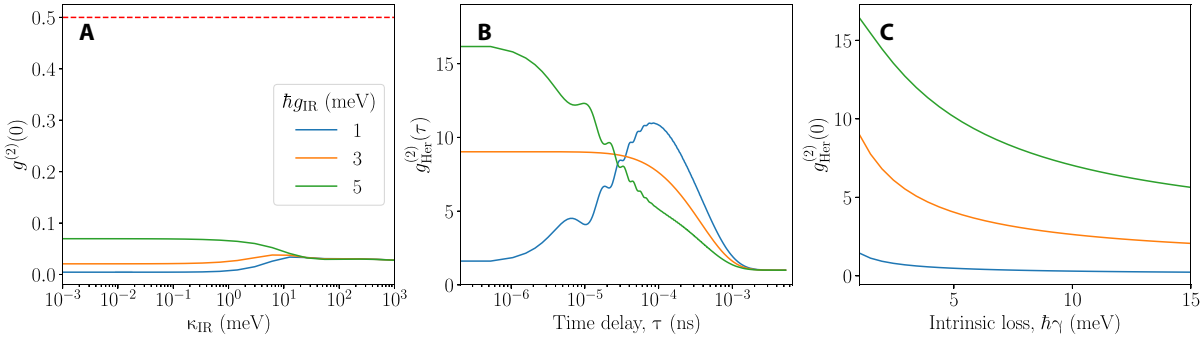

Fig. 4. Correlations of photons emitted from the MIR cavity. (**A**) A graph showing the degree of antibunching for the MIR photon emission calculated from Eq. 13 as a function of the MIR cavity losses and for several different values of the MIR coupling given in the legend and $\hbar\gamma = 10$ meV. The dashed red curve shows the classical limit. (**B**) The correlations between the heralding photon and the MIR photon emission as a function of time delay with intrinsic loss $\hbar\gamma = 1$ meV, and different values of $\hbar g_{\mathrm{IR}}$ matching those used in (A). (**C**) shows the change in the heralding efficiency as a function of intrinsic loss of the phonon mode. All other parameters used match those of Fig. 3.

oscillation pattern, the single excitation amplitude is critical to determining the effective dipole moment of a single phonon excitation. In line with our Frank-Condon model of the phonon modes, we will extract the single-phonon displacement amplitude via the well-known result for the quantum harmonic oscillator, which states that

$$\langle n|\hat{x}_\nu^2|n\rangle = (2n+1)\frac{\hbar}{2\mu_R\omega} \tag{16}$$

where μ_R is the reduced ion mass of the lattice, ω is the characteristic frequency of oscillator, and $|n\rangle$ is the nth vibrational eigenstate of the harmonic oscillator. Because we are interested in a single phonon mode, we take $n = 1$.

Next we consider the bounds of the effective dipole moment. The lower bound of the induced dipole moment is simply 0 debye (D). This is because even in a highly polar lattice, some vibration patterns will result in zero net movement of charge. The upper bound is more challenging to obtain because it will generally depend both on the material system and on a specific phonon mode.

The paradigmatic polar phonon modes in bulk systems are the longitudinal optical (LO) and transverse optical (TO) phonon modes. These modes are characterized by the anion and cation of the lattice oscillating in opposite directions, along the direction of propagation (LO) and transverse to the direction of propagation (TO). In simple binary crystals, we can thus state that $\varepsilon_{\text{anion}} = -\varepsilon_{\text{cation}}$. We will use these prototypical phonon modes to set the upper bound by assuming that the maximum achievable single-phonon dipole moment is the same as the polarization of a single TO mode excitation in the primitive bulk unit cell

$$|\mu_N| = \left(|Z_{\text{cation}}| + |Z_{\text{anion}}|\right)\left(\frac{3\hbar}{2\mu_R\omega}\right)^{1/2} \tag{17}$$

Color centers in hBN

We will first discuss color centers in hBN. hBN is a popular host material for color centers producing single photons in the visible (*54*–*57*), which naturally hosts polar phonon modes due to the polar nature of its lattice (*58*, *59*). For a PSB of interest, one would calculate the Born effective charges and phonon modes of the lattice with the defect included. Equation 15 would then be used to determine whether the oscillation pattern of the phonon mode responsible for the relevant sideband is such that an overall polarization change occurs. The induced polarization is thus generally both color center and phonon mode specific. Because the number of defect-host material combinations is extremely large, we will refrain from considerations of specific defects in this work and instead use Eq. 17 to estimate the upper limit of the achievable dipole moments. In pristine monolayer hBN, the boron atoms have a Born effective charge of $Z_B = 2.71e$ for displacements in plane, and the nitrogen atoms have an effective Born charge of $Z_N = -2.71e$; note that $\sum_\alpha Z_\alpha = 0$, as expected. For the frequency, we will use the LO/TO energy of monolayer hBN of around 170 meV. As shown in Table 1, inserting these values into Eq. 17 leads to an effective dipole moment of 1.04 D.

Another important quantity when considering the conversion efficiency of a particular emitter is the lifetime of the phonon mode. For defect centers in hBN, the linewidths reported for PSBs vary substantially depending on the quality of the sample and the phonon mode in question. We refer the reader to table S4 for a comparison of these modes; however, reported linewidths can be found in the range $\hbar\gamma = 0.33$ to 2.6 meV (*30*, *60*). Following Fig. 3, this suggests that high operating efficiencies are possible so long as IR coupling strengths are sufficiently large.

Table 1. Comparing material platforms based on the bulk TO mode frequencies. Effective dipole moment for single-phonon excitations in different material platforms with bulk TO phonon frequencies and Born effective charges calculated using density functional theory.

Material platform	Effective dipole moment
Bulk InP estimate (LO/TO)	1.05 D
Bulk hBN estimate (LO/TO)	1.04 D
Bulk CdS estimate (LO/TO)	0.9 D
Benzene [pyrene ref. (*25*)]	0.11 D

Colloidal quantum dots

Colloidal quantum dots are another interesting platform for the scheme we envision. In particular, in addition to strong coupling to acoustic sidebands, the emission spectra of InP/ZnSe QDs show clear signs of coupling to the LO/TO mode of the InP crystal in the form of a sideband around 45 meV from the ZPL (*61*, *62*). When calculating the Born effective charges, these come out to $2.6e$ and $-2.6e$ for In and P, respectively. Performing the same analysis as for hBN, we thus arrive at an effective dipole moment of 1.05 D. Here, note that unlike the color centers, the QDs actually contain bulk InP. It is therefore reasonable to expect this estimate for bulk InP to be a good measure of what one would measure with a real QD.

Giant shell CdS/Cd colloidal quantum dots display interesting quantum optical properties (*63*, *64*). These materials also host optical phonon modes featuring high dipole moments (see Table 1). Strong coupling between optically active (surface) phonon modes in CdS and metallic antenna resonant at terahertz (THz) frequencies has been demonstrated recently (*65*), thereby also demonstrating the feasibility to couple efficiently nanocrystals with optical antennas at these frequencies. Calculating the Born effective charges of CdS leads to $2.1e$ and $-2.1e$ for the Cd and S atoms, respectively. Following the same approach as outlined above, we find a dipole moment of 0.9 D. We note that this number is around an order of magnitude lower than the dipole moment of 17 D that one can extract from the experiment in (*65*). This emphasizes that more polar modes than the bulk ones can exist near surfaces (and potentially in defects such as in hBN).

Similar to the case of hBN, the linewidths of phonon modes within colloidal quantum dots vary substantially depending on the sample composition and size of the colloidal system. To give an indicative value, PSB linewidths of ≈ 3 meV at 4 K have been reported by Brodu *et al.* (*61*) in InP QDs.

Organic molecules

Last, for comparison, we consider IR active modes in organic molecules such as methylene blue or PAA where the dipole moment of the IR active mode can range from 0.1 D (*19*) to almost 0.5 D (*25*), respectively. As a model organic molecule, we calculate the effective charges of the atoms in a benzene molecule. Our calculations show a maximum effective charge of $0.13e$ and $-0.13e$ for the hydrogen

and carbon atoms, respectively, which is notably lower than for the inorganic crystals. Following the same procedure as above for the inorganic crystals, we estimate a dipole moment of 0.11 D as the upper bound for the optically active phonons in benzene. This dipole moment is an order of magnitude lower than for the III to V materials and hBN. Though the dipole moment of the phonon mode is lower than those found in polar crystalline materials, phonon lifetimes in molecular system can be much longer than their solid-state counterparts. For example, dibenzoterrylene, a stable organic molecule QE (*34*), has been reported to have PSB linewidths as narrow as = 0.016 meV (*66*), therefore requiring much lower coupling strengths to the IR antenna to obtain high conversion efficiencies.

Extracting antenna-phonon coupling strength

Given the dipole moment of a material system, we can estimate the expected antenna-phonon coupling strength using Eq. 6. Assuming the dipole moment of the phonon is parallel to the field, we obtain $\hbar g_{IR} = \sqrt{\hbar\omega_{IR}/2}\,|\mu_N||\lambda_{IR}|$. This coupling strength will be dependent on the mode volume, V_m, of the antenna structure through the equation $|\lambda_N| \approx 1/\sqrt{\varepsilon\varepsilon_0 V_m}$, where ε_0 (ε) is the vacuum (material) permittivity and V_m is the mode volume. Figure 5 shows the coupling strength as a function of mode volume for phonon dipole moments characteristic of solid-state and molecular systems. Our analysis here suggests that III to V materials as well as highly polar 2D materials such as hBN are promising platforms for the transduction process proposed in this work.

This analysis also reveals that for mode volumes around 5 to 20 nm^3, coupling strengths of $\hbar g_{IR} \approx 10$ meV and $\hbar g_{IR} \approx 5$ meV, respectively, can be achieved. Such coupling strengths should enable efficient phonon–to–MIR photon conversion, as discussed in the next section. Achieving small mode volumes at MIR frequencies is challenging, but recent advances in hybrid metal-graphene antennas using acoustic graphene plasmons have demonstrated light confinement with mode volumes around 200 nm^3 (*67*). This level of confinement already enables antenna-phonon couplings of approximately 1.6 meV for a dipole moment of the phonon around 1 D (see table S5). Further developments with hyperbolic phonon-polaritons could reduce mode volumes to just a few cubic nanometers. Recent near-field measurements on boron nitride nanotubes (*68*) have achieved mode volumes as small as 25 nm^3 at MIR frequencies, suggesting that coupling strengths of 5 to 10 meV are experimentally feasible (see table S5). In addition, computer-aided design techniques, such as topology optimization (*45*–*49*), could further enhance phonon-antenna confinement to maximize coupling strength and conversion efficiency.

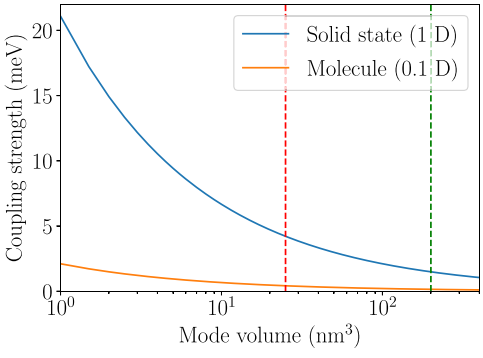

Fig. 5. Antenna-phonon coupling strength as a function of mode volume. The expected coupling strength for phonon modes with dipole moments characteristic of solid-state (1 D) and molecular (0.1 D) systems. For both systems, we have chosen a material permittivity of 1.5 and a phonon mode with energy $\hbar\omega_{IR} = 170$ meV. We have indicated the current state of the mode volumes for hybrid metal-graphene antennas (*67*) and boron nitride nanotubes (*68*) using the dashed green and red lines, respectively.

Estimating protocol efficiency for realistic QEs

For completeness, we now estimate the total efficiency of our scheme based on realistic parameters for the cavity and the MIR antenna, using an illustrative QE. As an example model system, we consider a QE in hBN as characterized in (*35*), with the central phonon mode in the first PSB—referred to as LO1 in table S4—chosen as the target phonon mode. The PSB corresponding to the optical transition to LO1 is centered at $E_{LO1} = 1871$ meV with a linewidth of $\Delta E_{LO1} = 2.2$ meV, which translates to a phonon intrinsic loss rate of 2.2 meV at a temperature of 8 K (see table S4). To selectively excite LO1 without exciting the closest mode LO1′′, the cavity must have a linewidth no larger than that of the energy separation between LO1 and LO1′′, which gives a quality factor of $Q_{Vis} = 1871/9 = 208$. Dielectric nanobeam cavity integrating plasmonic dimers in the cavity reaching quality factors of similar amplitude have already been demonstrated by Shlesinger *et al.* (*69*). If we assume a coupling strength between the QE and the cavity on the order of $g_{Vis} = 0.75$ meV (*70*) as shown in Fig. 2, then we will have a peak phonon occupation 0.3, which we take as a lower bound for the phonon generation efficiency P_{gen}.

Once the single phonon Fock state is generated, it must be converted into a MIR photon before being lost to nonradiative processes. This requires operation in the critical coupling regime (*42*), where the radiative rate of the antenna (Γ_R) is greater than both the nonradiative rate (Γ_{NR}) and the antenna-phonon coupling rate (g_{IR}), as well as the phonon mode's internal decay rate (γ), to avoid energy backflow to the phonon modes or nonradiative losses. For an antenna with $\hbar\Gamma_R = 50$ meV, $\hbar\Gamma_{NR} = 15$ meV (see table S3), a coupling rate $\hbar g_{IR} = 10$ meV (see Fig. 5), and assuming a phonon intrinsic loss rate of $\hbar\gamma = 2.2$ meV (see table S4), a conversion efficiency of $\varepsilon = 0.65$ can be achieved. Antennas with comparable parameters have already been reported in the literature (*18*, *42*, *44*, *71*).

The estimated total efficiency in our example is the product of the phonon generation efficiency and the phonon-to-photon conversion efficiency, yielding $\eta_{total} = P_{gen}\varepsilon \approx 0.2$. While this value may not seem high, it is important to emphasize that P_{gen} is a lower bound on the generation efficiency and the antenna parameters used from the literature are not optimized for our scheme. For instance, inverse design techniques and topology optimization (*45*, *48*) could be used to minimize antenna scattering when integrated into the cavity. By optimizing the quality factor and reducing the mode volume, stronger QE-cavity coupling could be achieved, leading to higher phonon generation efficiency (see Fig. 2D). In addition, antennas designed using dielectric materials like hBN could reduce nonradiative losses while maximizing the radiative rate, thereby increasing phonon–to–MIR photon conversion efficiency. Materials with low internal phonon losses, such as isotopically pure materials (*60*) (see table S4), could further improve conversion efficiency, potentially reaching $\varepsilon \approx 0.75$ for isotopically pure hBN.

Last, we note that in our scheme, the generation of a MIR photon is heralded by the detection of a photon emitted at the first PSB. The detection of this heralding photon in the visible—where detector technology is now highly advanced—could substantially enhance

the detection efficiency of the correlated MIR photon. This approach would be particularly beneficial for applications in quantum spectroscopy at MIR frequencies (*72*).

DISCUSSION

In this work, we have demonstrated a unique mechanism to efficiently and quasi-deterministically generate heralded single photons at MIR and even THz frequencies. The parameters required for our protocol, including optical transition energies, photonic cavities, optical phonon modes, and MIR antenna coupling strengths, are all realistic and achievable with state-of-the-art materials and nanofabrication. For example, coupling amplitudes between optical transitions in QE and nanocavities can reach the tens of milli–electron volts regime (*73*, *74*), and coupling strength between optical phonon modes and MIR-THz antennas of several milli–electron volts have been demonstrated experimentally (*65*). Double antenna devices featuring resonances at visible and MIR frequencies have been proposed theoretically (*20*) and demonstrated experimentally (*44*, *71*). Such a design would allow emission rate enhancement of the optical transitions at the first PSB while allowing to convert single polar phonons into MIR photons sent to the far field. We are therefore confident that our scheme is within reach experimentally using existing technologies.

Our scheme is versatile and may be realized with a wide range of material systems. In particular, polar materials such as low-dimensional hBN and 3D bulk III to V materials host optical phonon modes with dipole moments one order of magnitude higher than for organic molecules, thus allowing more efficient coupling to dielectric or metallic antennas. Our scheme can also be applied to the generation of single polaritons propagating at the surface of materials (*75*–*77*), as long as the degrees of freedom of the polarization wave couple strongly to localized electrons or excitons in QEs. The strong correlation between the single photon emitted in the visible and in the MIR works as an interface between the MIR-THz and the visible-NIR regimes, thereby opening the possibility for quasi-deterministic transduction protocols and could be used in high-fidelity quantum measurements (*78*).

Overall, our proposed design for heralded QEs at MIR and THz frequencies could enable the creation of innovative spectroscopic methods at the single photon and single phonon level. This has the potential to enhance our understanding of quantum phenomena in molecular biology and in quantum materials where optical phonons play a prominent role.

Supplementary Materials

This PDF file includes:

Supplementary text
Tables S1 to S5
Fig. S1
References

REFERENCES AND NOTES

1. E. Jakeman, J. Rarity, The use of pair production processes to reduce quantum noise in transmission measurements. *Optics Commun.* **59**, 219–223 (1986).
2. G. Adesso, F. Dell'Anno, S. De Siena, F. Illuminati, L. A. M. Souza, Optimal estimation of losses at the ultimate quantum limit with non-Gaussian states. *Phys. Rev. A* **79**, 040305 (2009).
3. R. Whittaker, C. Erven, A. Neville, M. Berry, J. L. O'Brien, H. Cable, J. C. F. Matthews, Absorption spectroscopy at the ultimate quantum limit from single-photon states. *New J. Phys.* **19**, 023013 (2017).
4. P.-A. Moreau, J. Sabines-Chesterking, R. Whittaker, S. K. Joshi, P. M. Birchall, A. McMillan, J. G. Rarity, J. C. F. Matthews, Demonstrating an absolute quantum advantage in direct absorption measurement. *Sci. Rep.* **7**, 6256 (2017).
5. M. A. Taylor, J. Janousek, V. Daria, J. Knittel, B. Hage, H. A. Bachor, W. P. Bowen, Biological measurement beyond the quantum limit. *Nat. Photonics* **7**, 229–233 (2013).
6. F. Wolfgramm, C. Vitelli, F. A. Beduini, N. Godbout, M. W. Mitchell, Entanglement-enhanced probing of a delicate material system. *Nat. Photonics* **7**, 28–32 (2013).
7. M. A. Taylor, W. P. Bowen, Quantum metrology and its application in biology. *Phys. Rep.* **615**, 1–59 (2016).
8. N. Samantaray, I. Ruo-Berchera, A. Meda, M. Genovese, Realization of the first sub-shot-noise wide field microscope. *Light Sci. Appl.* **6**, e17005–e17005 (2017).
9. D. Basov, R. Averitt, D. Hsieh, Towards properties on demand in quantum materials. *Nat. Mater.* **16**, 1077–1088 (2017).
10. K. Heyne, O. Kühn, Infrared laser excitation controlled reaction acceleration in the electronic ground state. *J. Am. Chem. Soc.* **141**, 11730–11738 (2019).
11. T. Stensitzki, Y. Yang, V. Kozich, A. A. Ahmed, F. Kössl, O. Kühn, K. Heyne, Acceleration of a ground-state reaction by selective femtosecond-infrared-laser-pulse excitation. *Nat. Chem.* **10**, 126–131 (2018).
12. D. A. Vajner, P. Holewa, E. Zięba-Ostój, M. Wasiluk, M. von Helversen, A. Sakanas, A. Huck, K. Yvind, N. Gregersen, A. Musiał, M. Syperek, E. Semenova, T. Heindel, On-demand generation of indistinguishable photons in the telecom C-band using quantum dot devices. *ACS Photonics* **11**, 339–347 (2024).
13. C. L. Phillips, A. J. Brash, M. Godsland, N. J. Martin, A. Foster, A. Tomlinson, R. Dost, N. Babazadeh, E. M. Sala, L. Wilson, J. Heffernan, M. S. Skolnick, A. M. Fox, Purcell-enhanced single photons at telecom wavelengths from a quantum dot in a photonic crystal cavity. *Sci. Rep.* **14**, 4450 (2024).
14. C. Galland, N. Sangouard, N. Piro, N. Gisin, T. J. Kippenberg, Heralded single-phonon preparation, storage, and readout in cavity optomechanics. *Phys. Rev. Lett.* **112**, 143602 (2014).
15. R. Riedinger, S. Hong, R. A. Norte, J. A. Slater, J. Shang, A. G. Krause, V. Anant, M. Aspelmeyer, S. Gröblacher, Non-classical correlations between single photons and phonons from a mechanical oscillator. *Nature* **530**, 313–316 (2016).
16. S. Hong, R. Riedinger, I. Marinković, A. Wallucks, S. G. Hofer, R. A. Norte, M. Aspelmeyer, S. Gröblacher, Hanbury Brown and Twiss interferometry of single phonons from an optomechanical resonator. *Science* **358**, 203–206 (2017).
17. S. T. Velez, K. Seibold, N. Kipfer, M. D. Anderson, V. Sudhir, C. Galland, Preparation and decay of a single quantum of vibration at ambient conditions. *Phys. Rev. X.* **9**, 041007 (2019).
18. M. A. Kats, N. Yu, P. Genevet, Z. Gaburro, F. Capasso, Effect of radiation damping on the spectral response of plasmonic components. *Opt. Express* **19**, 21748–21753 (2011).
19. R. Chikkaraddy, R. Arul, L. A. Jakob, J. J. Baumberg, Single-molecule mid-infrared spectroscopy and detection through vibrationally assisted luminescence. *Nat. Photonics* **17**, 865–871 (2023).
20. P. Roelli, D. Martin-Cano, T. J. Kippenberg, C. Galland, Molecular platform for frequency upconversion at the single-photon level. *Phys. Rev. X.* **10**, 031057 (2020).
21. L. Novotny, N. van Hulst, Antennas for light. *Nat. Photonics* **5**, 83–90 (2011).
22. P. Biagioni, J.-S. Huang, B. Hecht, Nanoantennas for visible and infrared radiation. *Rep. Prog. Phys.* **75**, 024402 (2012).
23. A. F. Koenderink, Single-photon nanoantennas. *ACS Photonics* **4**, 710–722 (2017).
24. J. T. Hugall, A. Singh, N. F. van Hulst, Plasmonic cavity coupling. *ACS Photonics* **5**, 43–53 (2018).
25. C. K. Terry Weatherly, J. Provazza, E. A. Weiss, R. Tempelaar, Theory predicts UV/Vis-to-IR photonic down conversion mediated by excited state vibrational polaritons. *Nat. Commun.* **14**, 4804 (2023).
26. C. Groiseau, A. I. Fernández-Domínguez, D. Martín-Cano, C. S. Muñoz, Single-photon source over the terahertz regime. *PRX Quantum* **5**, 010312 (2024).
27. F. H. Faisal, *Theory of Multiphoton Processes* (Springer Science & Business Media, 1987).
28. I. V. Tokatly, Time-dependent density functional theory for many-electron systems interacting with cavity photons. *Phys. Rev. Lett.* **110**, 233001 (2013).
29. M. K. Svendsen, K. S. Thygesen, A. Rubio, J. Flick, Ab initio calculations of quantum light–matter interactions in general electromagnetic environments. *J. Chem. Theory Comput.* **20**, 926–936 (2024).
30. C. Schäfer, M. Ruggenthaler, V. Rokaj, A. Rubio, Relevance of the quadratic diamagnetic and self-polarization terms in cavity quantum electrodynamics. *ACS Photonics* **7**, 975–990 (2020).
31. B. J. Dalton, S. M. Barnett, B. M. Garraway, Theory of pseudomodes in quantum optical processes. *Phys. Rev. A* **64**, 053813 (2001).
32. D. Tamascelli, A. Smirne, S. F. Huelga, M. B. Plenio, Nonperturbative treatment of non-Markovian dynamics of open quantum systems. *Phys. Rev. Lett.* **120**, 030402 (2018).
33. G. Pleasance, B. M. Garraway, F. Petruccione, Generalized theory of pseudomodes for exact descriptions of non-Markovian quantum processes. *Phys. Rev. Res.* **2**, 043058 (2020).
34. C. Clear, R. C. Schofield, K. D. Major, J. Iles-Smith, A. S. Clark, D. P. S. McCutcheon, Phonon-induced optical dephasing in single organic molecules. *Phys. Rev. Lett.* **124**, 153602 (2020).
35. J. A. Preuss, D. Groll, R. Schmidt, T. Hahn, P. Machnikowski, R. Bratschitsch, T. Kuhn, S. Michaelis de Vasconcellos, D. Wigger, Resonant and phonon-assisted ultrafast coherent control of a single hBN color center. *Optica* **9**, 522–531 (2022).

36. T. K. Bracht, M. Cosacchi, T. Seidelmann, M. Cygorek, A. Vagov, V. M. Axt, T. Heindel, D. E. Reiter, Swing-up of quantum emitter population using detuned pulses. *PRX Quantum* **2**, 040354 (2021).
37. Y. Karli, F. Kappe, V. Remesh, T. K. Bracht, J. Münzberg, S. Covre da Silva, T. Seidelmann, V. M. Axt, A. Rastelli, D. E. Reiter, G. Weihs, Super scheme in action: Experimental demonstration of red-detuned excitation of a quantum emitter. *Nano Lett.* **22**, 6567–6572 (2022).
38. C. G. Torun, M. Gökçe, T. K. Bracht, M. I. Monsalve, S. Benbouabdellah, Ö. O. Nacitarhan, M. E. Stucki, M. L. Markham, G. Pieplow, T. Pregnolato, J. H. D. Munns, D. E. Reiter, T. Schröder, SUPER and subpicosecond coherent control of an optical qubit in a tin-vacancy color center in diamond. arXiv:2312.05246 [quant-ph] (2023).
39. N. Somaschi, V. Giesz, L. de Santis, J. C. Loredo, M. P. Almeida, G. Hornecker, S. L. Portalupi, T. Grange, C. Antón, J. Demory, C. Gómez, I. Sagnes, N. D. Lanzillotti-Kimura, A. Lemaître, A. Auffeves, A. G. White, L. Lanco, P. Senellart, Near-optimal single-photon sources in the solid state. *Nat. Photonics* **10**, 340–345 (2016).
40. T. Grange, N. Somaschi, C. Antón, L. de Santis, G. Coppola, V. Giesz, A. Lemaître, I. Sagnes, A. Auffèves, P. Senellart, Reducing phonon-induced decoherence in solid-state single-photon sources with cavity quantum electrodynamics. *Phys. Rev. Lett.* **118**, 253602 (2017).
41. J. Iles-Smith, D. P. S. McCutcheon, A. Nazir, J. Mørk, Phonon scattering inhibits simultaneous near-unity efficiency and indistinguishability in semiconductor single-photon sources. *Nat. Photonics* **11**, 521–526 (2017).
42. P. Roelli, H. Hu, E. Verhagen, S. Reich, C. Galland, Nanocavities for molecular optomechanics: Their fundamental description and applications. *ACS Photonics* **11**, 4486–4501 (2024).
43. J. J. Baumberg, J. Aizpurua, M. H. Mikkelsen, D. R. Smith, Extreme nanophotonics from ultrathin metallic gaps. *Nat. Mater.* **18**, 668–678 (2019).
44. A. Xomalis, X. Zheng, R. Chikkaraddy, Z. Koczor-Benda, E. Miele, E. Rosta, G. A. E. Vandenbosch, A. Martínez, J. J. Baumberg, Detecting mid-infrared light by molecular frequency upconversion in dual-wavelength nanoantennas. *Science* **374**, 1268–1271 (2021).
45. M. Albrechtsen, B. Vosoughi Lahijani, R. E. Christiansen, V. T. H. Nguyen, L. N. Casses, S. E. Hansen, N. Stenger, O. Sigmund, H. Jansen, J. Mørk, S. Stobbe, Nanometer-scale photon confinement in topology-optimized dielectric cavities. *Nat. Commun.* **13**, 6281 (2022).
46. M. Xiong, R. E. Christiansen, F. Schröder, Y. Yu, L. N. Casses, E. Semenova, K. Yvind, N. Stenger, O. Sigmund, J. Mørk, Experimental realization of deep sub-wavelength confinement of light in a topology-optimized InP nanocavity. *Opt. Mater. Express* **14**, 397–406 (2024).
47. H. Choi, M. Heuck, D. Englund, Self-similar nanocavity design with ultrasmall mode volume for single-photon nonlinearities. *Phys. Rev. Lett.* **118**, 223605 (2017).
48. F. Wang, R. E. Christiansen, Y. Yu, J. Mørk, O. Sigmund, Maximizing the quality factor to mode volume ratio for ultra-small photonic crystal cavities. *Appl. Phys. Lett.* **113**, 241101 (2018).
49. S. Mignuzzi, S. Vezzoli, S. A. R. Horsley, W. L. Barnes, S. A. Maier, R. Sapienza, Nanoscale design of the local density of optical states. *Nano Lett.* **19**, 1613–1617 (2019).
50. R. Resta, D. Vanderbilt, Theory of polarization: A modern approach, in *Physics of Ferroelectrics: A Modern Perspective* (Springer, 2007), pp. 31–68.
51. J. Enkovaara, C. Rostgaard, J. J. Mortensen, J. Chen, M. Dułak, L. Ferrighi, J. Gavnholt, C. Glinsvad, V. Haikola, H. A. Hansen, H. H. Kristoffersen, M. Kuisma, A. H. Larsen, L. Lehtovaara, M. Ljungberg, O. Lopez-Acevedo, P. G. Moses, J. Ojanen, T. Olsen, V. Petzold, N. A. Romero, J. Stausholm-Møller, M. Strange, G. A. Tritsaris, M. Vanin, M. Walter, B. Hammer, H. Häkkinen, G. K. H. Madsen, R. M. Nieminen, J. K. Nørskov, M. Puska, T. T. Rantala, J. Schiøtz, K. S. Thygesen, K. W. Jacobsen, Electronic structure calculations with GPAW: A real-space implementation of the projector augmented-wave method. *J. Phys. Condens. Matter* **22**, 253202 (2010).
52. A. H. Larsen, J. J. Mortensen, J. Blomqvist, I. E. Castelli, R. Christensen, M. Dułak, J. Friis, M. N. Groves, B. Hammer, C. Hargus, E. D. Hermes, P. C. Jennings, P. B. Jensen, J. Kermode, J. R. Kitchin, E. L. Kolsbjerg, J. Kubal, K. Kaasbjerg, S. Lysgaard, J. B. Maronsson, T. Maxson, T. Olsen, L. Pastewka, A. Peterson, C. Rostgaard, J. Schiøtz, O. Schütt, M. Strange, K. S. Thygesen, T. Vegge, L. Vilhelmsen, M. Walter, Z. Zeng, K. W. Jacobsen, The atomic simulation environment—A Python library for working with atoms. *J. Phys. Condens. Matter* **29**, 273002 (2017).
53. J. J. Mortensen, A. H. Larsen, M. Kuisma, A. V. Ivanov, A. Taghizadeh, A. Peterson, A. Haldar, A. O. Dohn, C. Schäfer, E. Ö. Jónsson, E. D. Hermes, F. A. Nilsson, G. Kastlunger, G. Levi, H. Jónsson, H. Häkkinen, J. Fojt, J. Kangsabanik, J. Sødequist, J. Lehtomäki, J. Heske, J. Enkovaara, K. T. Winther, M. Dulak, M. M. Melander, M. Ovesen, M. Louhivuori, M. Walter, M. Gjerding, O. Lopez-Acevedo, P. Erhart, R. Warmbier, R. Würdemann, S. Kaappa, S. Latini, T. M. Boland, T. Bligaard, T. Skovhus, T. Susi, T. Maxson, T. Rossi, X. Chen, Y. L. A. Schmerwitz, J. Schiøtz, T. Olsen, K. W. Jacobsen, K. S. Thygesen, GPAW: An open Python package for electronic structure calculations. *J. Chem. Phys.* **160**, 092503 (2024).
54. T. T. Tran, K. Bray, M. J. Ford, M. Toth, I. Aharonovich, Quantum emission from hexagonal boron nitride monolayers. *Nat. Nanotechnol.* **11**, 37–41 (2016).
55. M. Fischer, J. M. Caridad, A. Sajid, S. Ghaderzadeh, M. Ghorbani-Asl, L. Gammelgaard, P. Bøggild, K. S. Thygesen, A. V. Krasheninnikov, S. Xiao, M. Wubs, N. Stenger, Controlled generation of luminescent centers in hexagonal boron nitride by irradiation engineering. *Sci. Adv.* **7**, eabe7138 (2021).
56. S. Michaelis de Vasconcellos, D. Wigger, U. Wurstbauer, A. W. Holleitner, R. Bratschitsch, T. Kuhn, Single-photon emitters in layered Van der Waals materials. *Phys. Status Solidi. A Appl. Mater. Sci.* **259**, 2100566 (2022).
57. I. Aharonovich, J.-P. Tetienne, M. Toth, Quantum emitters in hexagonal boron nitride. *Nano Lett.* **22**, 9227–9235 (2022).
58. D. Wigger, R. Schmidt, O. del Pozo-Zamudio, J. A. Preuß, P. Tonndorf, R. Schneider, P. Steeger, J. Kern, Y. Khodaei, J. Sperling, S. M. de Vasconcellos, R. Bratschitsch, T. Kuhn, Phonon-assisted emission and absorption of individual color centers in hexagonal boron nitride. *2D Mat.* **6**, 035006 (2019).
59. M. Fischer, A. Sajid, J. Iles-Smith, A. Hötger, D. I. Miakota, M. K. Svendsen, C. Kastl, S. Canulescu, S. Xiao, M. Wubs, K. S. Thygesen, A. W. Holleitner, N. Stenger, Combining experiments on luminescent centres in hexagonal boron nitride with the polaron model and ab initio methods towards the identification of their microscopic origin. *Nanoscale* **15**, 14215–14226 (2023).
60. R. Cuscó, L. Artús, J. H. Edgar, S. Liu, G. Cassabois, B. Gil, Isotopic effects on phonon anharmonicity in layered van der Waals crystals: Isotopically pure hexagonal boron nitride. *Phys. Rev. B* **97**, 155435 (2018).
61. A. Brodu, M. V. Ballottin, J. Buhot, E. J. van Harten, D. Dupont, A. la Porta, P. T. Prins, M. D. Tessier, M. A. M. Versteegh, V. Zwiller, S. Bals, Z. Hens, F. T. Rabouw, P. C. M. Christianen, C. de Mello Donega, D. Vanmaekelbergh, Exciton fine structure and lattice dynamics in InP/ZnSe core/shell quantum dots. *ACS Photonics* **5**, 3353–3362 (2018).
62. A. H. Proppe, D. B. Berkinsky, H. Zhu, T. Šverko, A. E. K. Kaplan, J. R. Horowitz, T. Kim, H. Chung, S. Jun, M. G. Bawendi, Highly stable and pure single-photon emission with 250 ps optical coherence times in InP colloidal quantum dots. *Nat. Nanotechnol.* **18**, 993–999 (2023).
63. Y. Chen, J. Vela, H. Htoon, J. L. Casson, D. J. Werder, D. A. Bussian, V. I. Klimov, J. A. Hollingsworth, Giant multishell CdSe nanocrystal quantum dots with suppressed blinking. *J. Am. Chem. Soc.* **130**, 5026–5027 (2008).
64. S. Morozov, S. Vezzoli, A. Myslovska, A. di Giacomo, N. A. Mortensen, I. Moreels, R. Sapienza, Purifying single photon emission from giant shell CdSe/CdS quantum dots at room temperature. *Nanoscale* **15**, 1645–1651 (2023).
65. X. Jin, A. Cerea, G. C. Messina, A. Rovere, R. Piccoli, F. de Donato, F. Palazon, A. Perucchi, P. di Pietro, R. Morandotti, S. Lupi, F. de Angelis, M. Prato, A. Toma, L. Razzari, Reshaping the phonon energy landscape of nanocrystals inside a terahertz plasmonic nanocavity. *Nat. Commun.* **9**, 763 (2018).
66. J. Zirkelbach, M. Mirzaei, I. Deperasińska, B. Kozankiewicz, B. Gurlek, A. Shkarin, T. Utikal, S. Götzinger, V. Sandoghdar, High-resolution vibronic spectroscopy of a single molecule embedded in a crystal. *J. Chem. Phys.* **156**, 104301 (2022).
67. I. Epstein, D. Alcaraz, Z. Huang, V. V. Pusapati, J. P. Hugonin, A. Kumar, X. M. Deputy, T. Khodkov, T. G. Rappoport, J. Y. Hong, N. M. R. Peres, J. Kong, D. R. Smith, F. H. L. Koppens, Far-field excitation of single graphene plasmon cavities with ultracompressed mode volumes. *Science* **368**, 1219–1223 (2020).
68. X. Guo, N. Li, X. Yang, R. Qi, C. Wu, R. Shi, Y. Li, Y. Huang, F. J. García de Abajo, E. G. Wang, P. Gao, Q. Dai, Hyperbolic whispering-gallery phonon polaritons in boron nitride nanotubes. *Nat. Nanotechnol.* **18**, 529–534 (2023).
69. I. Shlesinger, I. M. Palstra, A. F. Koenderink, Integrated sideband-resolved SERS with a dimer on a nanobeam hybrid. *Phys. Rev. Lett.* **130**, 016901 (2023).
70. D. G. Baranov, M. Wersall, J. Cuadra, T. J. Antosiewicz, T. Shegai, Novel nanostructures and materials for strong light–matter interactions. *ACS Photonics* **5**, 24–42 (2018).
71. W. Chen, P. Roelli, H. Hu, S. Verlekar, S. P. Amirtharaj, A. I. Barreda, T. J. Kippenberg, M. Kovylina, E. Verhagen, A. Martínez, C. Galland, Continuous-wave frequency upconversion with a molecular optomechanical nanocavity. *Science* **374**, 1264–1267 (2021).
72. D. A. Kalashnikov, A. V. Paterova, S. P. Kulik, L. A. Krivitsky, Infrared spectroscopy with visible light. *Nat. Photonics* **10**, 98–101 (2016).
73. K.-D. Park, M. A. May, H. Leng, J. Wang, J. A. Kropp, T. Gougousi, M. Pelton, M. B. Raschke, Tip-enhanced strong coupling spectroscopy, imaging, and control of a single quantum emitter. *Sci. Adv.* **5**, 47 (2019).
74. H. Groß, J. M. Hamm, T. Tufarelli, O. Hess, B. Hecht, Near-field strong coupling of single quantum dots. *Sci. Adv.* **4**, eaar4906 (2018).
75. D. Basov, M. Fogler, F. García de Abajo, Polaritons in van der Waals materials. *Science* **354**, aag1992 (2016).
76. T. Low, A. Chaves, J. D. Caldwell, A. Kumar, N. X. Fang, P. Avouris, T. F. Heinz, F. Guinea, L. Martin-Moreno, F. Koppens, Polaritons in layered two-dimensional materials. *Nat. Mater.* **16**, 182–194 (2017).
77. D. N. Basov, A. Asenjo-Garcia, P. J. Schuck, X. Zhu, A. Rubio, Polariton panorama. *Nanophotonics* **10**, 549–577 (2020).

78. M. Kutas, B. E. Haase, F. Riexinger, J. Hennig, P. Bickert, T. Pfeiffer, M. Bortz, D. Molter, G. von Freymann, Quantum sensing with extreme light. *Adv. Quantum Technol.* **5**, 2100164 (2022).
79. M. Ruggenthaler, J. Flick, C. Pellegrini, H. Appel, I. V. Tokatly, A. Rubio, Quantum-electrodynamical density-functional theory: Bridging quantum optics and electronic-structure theory. *Phys. Rev. A* **90**, 012508 (2014).
80. A. N. Babar, T. A. S. Weis, K. Tsoukalas, S. Kadkhodazadeh, G. Arregui, B. Vosoughi Lahijani, S. Stobbe, Self-assembled photonic cavities with atomic-scale confinement. *Nature* **624**, 57–63 (2023).
81. C. Qian, V. Villafañe, M. Schalk, G. V. Astakhov, U. Kentsch, M. Helm, P. Soubelet, N. P. Wilson, R. Rizzato, S. Mohr, A. W. Holleitner, D. B. Bucher, A. V. Stier, J. J. Finley, Unveiling the zero-phonon line of the boron vacancy center by cavity-enhanced emission. *Nano Lett.* **22**, 5137–5142 (2022).
82. M. Nonahal, J. Horder, A. Gale, L. Ding, C. Li, M. Hennessey, S. T. Ha, M. Toth, I. Aharonovich, Deterministic fabrication of a coupled cavity-emitter system in hexagonal boron nitride. *Nano Lett.* **23**, 6645–6650 (2023).
83. J. D. Caldwell, A. V. Kretinin, Y. Chen, V. Giannini, M. M. Fogler, Y. Francescato, C. T. Ellis, J. G. Tischler, C. R. Woods, A. J. Giles, M. Hong, K. Watanabe, T. Taniguchi, S. A. Maier, K. S. Novoselov, Sub-diffractional volume-confined polaritons in the natural hyperbolic material hexagonal boron nitride. *Nat. Commun.* **5**, 5221 (2014).

Acknowledgments: We thank M. Fischer for stimulating discussions regarding the manuscript. **Funding:** This work was supported by the Danish National Research Foundation through the Center for Nanostructured Graphene (project number DNRF103) and through NanoPhoton-Center for Nanophotonics (project number DNRF147). N.S. acknowledges support from the VILLUM FONDEN (project number 00028233). N.S. and J.I.-S. thank the Novo Nordisk Foundation NERD Programme (project QuDec NNF23OC0082957) for financial support. N.S. and M.W. acknowledge support from the Independent Research Fund Denmark, Natural Sciences (project number 0135-00403B). M.K.S. and A.R. are supported by the Cluster of Excellence "CUI:Advanced Imaging of Matter" of the Deutsche Forschungsgemeinschaft (DFG) (EXC 2056 and SFB925), EXC 2056, Grupos Consolidados (IT1453-22), and SFB925. The Flatiron Institute is a division of the Simons Foundation. M.K.S. acknowledges support from the Novo Nordisk Foundation, grant number NNF22SA0081175, NNF Quantum Computing Programme. **Author contributions:** N.S., J.I.-S., M.K.S., and M.W. conceived the idea. J.I.-S., M.K.S., A.R., M.W., and N.S. discussed the model Hamiltonian of the cascaded quantum system. M.K.S. and J.I.-S. derived the model Hamiltonian. J.I.-S. performed the calculations of the dynamics of the cascaded quantum system. M.K.S. performed the ab initio calculations of the dipole moments of different material platforms. All authors discussed the results and participated in the writing of the manuscript. **Competing interests:** The authors declare that they have no competing interests. **Data and materials availability:** All data needed to evaluate the conclusions in the paper are present in the paper and/or the Supplementary Materials.

Submitted 23 July 2024
Accepted 5 February 2025
Published 12 March 2025
10.1126/sciadv.adr9239